Robust UAV Thermal Infrared Remote Sensing Images Stitching Via Overlap-Prior-Based Global Similarity Prior Model

Jiguang Cui, Man Liu, Zhitao Zhang, Shuqin Yang, and Jifeng Ning

***Abstract*—The main problem of stitching unmanned aerial vehicle (UAV) thermal infrared remote sensing (TIRS) images lies in that the cumulative error caused by the inaccurate alignment of image matching pairs easily leads to deformation and even failure. Few studies in the literature are reported in stitching TIRS images. For the first time, we propose a simple and robust TIRS image stitching method by exploring prior information during flight. First, according to the position and orientation system information and parameter of camera, the overlap ratio of adjacent images is estimated, and the image pairs with high overlap ratio and high matching confidence in different directions are selected. Then, they are added into the alignment term of global similarity prior (GSP) model. Therefore, each image has more matching pairs constraints compared to the traditional construction method of matching pairs, which greatly improves the local registration capability of GSP and then prevents it from converging to the local optimal solution. The proposed method was extensively evaluated on a dataset including to 24 groups of large-scale farmland TIRS images collected in four experimental areas under different crop growth periods and meteorological conditions. Compared with two commercial tools and two representative stitching algorithms, the proposed method significantly improves the local alignment ability and overall stitching quality on both qualitative and quantitative evaluation. Besides, when the front overlap ratio is reduced from 85% to 70%, the proposed method still shows obvious advantages over the related methods and commercial tools, which improves the acquisition efficiency of UAV TIRS images.**

***Index Terms*—Image stitching, overlap ratio prior, thermal infrared remote sensing (TIRS), unmanned aerial vehicle (UAV).**

Manuscript received August 12, 2020; revised September 24, 2020; accepted October 8, 2020. Date of publication October 19, 2020; date of current version January 6, 2021. This work was supported in part by the National Natural Science Foundation of China under Grant 61876153, in part by the National Key Research and Development Program of China under Grant 2016YFD0200700 and Grant 2017YFC0403302, and in part by the Fundamental Research Funds for the Central Universities under Grant 2452019180. *(Corresponding author: Jifeng Ning.)*

Jiguang Cui and Man Liu are with the College of Information Engineering, Northwest A&F University, Yangling 712100, China (e-mail: cuijiguang1997@163.com; mellthebs@nwafu.edu.cn).

Zhitao Zhang is with the College of Water Resources and Architectural Engineering, Northwest A&F University, Yangling 712100, China (e-mail: zhitaozhang@126.com).

Shuqin Yang is with the College of Mechanical and Electronic Engineering, Northwest A&F University, Yangling 712100, China, with the Key Laboratory of Agricultural Internet of Things, Ministry of Agriculture and Rural Affairs, Yangling 712100, China, and also with the Shaanxi Key Laboratory of Agricultural Information Perception and Intelligent Service, Yangling 712100, China (e-mail: yangshuqin1978@163.com).

Jifeng Ning is with the College of Information Engineering, Northwest A&F University, Yangling 712100, China, with the Key Laboratory of Agricultural Internet of Things, Ministry of Agriculture and Rural Affairs, Yangling 712100, China, and also with the Shaanxi Key Laboratory of Agricultural Information Perception and Intelligent Service, Yangling 712100, China (e-mail: njf@nwsuaf.edu.cn).

This article has supplementary downloadable material available at https://ieeexplore.ieee.org, provided by the authors.

Digital Object Identifier 10.1109/JSTARS.2020.3032011

I. Introduction

IMAGE stitching is a process of fusing multiple images into a panoramic image with a wide field of view (FOV) [1]. Unmanned aerial vehicle (UAV) thermal infrared remote sensing (TIRS) allows us to obtain spatially distributed and geometrically high-resolution information on the ground surface temperature [2], which brings new means for many research work. Specifically, the panoramic thermal infrared image of the research region base on UAV remote sensing via stitching technology can obtain the fine temperature information of ground, crop canopy, and field soil. They recently show a wide range of applications such as soil water balance assessment, water stress [3]–[5], mapping evaporation and canopy conductance [6]–[8], crop lodging identification [9], fine research of urban thermal environment [10], [11], and real-time ground vehicle semantic segmentation [12].

The panoramic thermal infrared image with high stitching quality in the study area is an important prerequisite for the above-related applications. There are already some commercial tools on the market, such as Pix4Dmapper [13] and PTGui [14], which can be used to stitch the UAV TIRS images. However, unlike visible and multispectral images, TIRS images are susceptible to wind and temperature drift [15] and have low geometric resolution, low signal-to-noise ratio, and poor quality [16]–[18], which poses a great challenge to robust stitching. For example, Fig. 1(a) and (b) illustrates a stitched results of a set of 100 TIRS images (85% front image overlap and 75% side image overlap) by using the commercial tools Pix4Dmapper and PTGui. We observed that although Pix4Dmapper can get a complete stitched result, the details of the panoramic image are poor, and there are obvious problems of uneven light and shade transition, and PTGui has serious stitched dislocation. Furthermore, it is worth noting that Pix4Dmapper and other commercial tools require the front overlap ratio to be greater than 85% when stitching the UAV TIRS images [19], which will reduce the acquisition efficiency of TIRS images.

Although the stitching of UAV TIRS images is very important, the research work in this field is very few, and the related

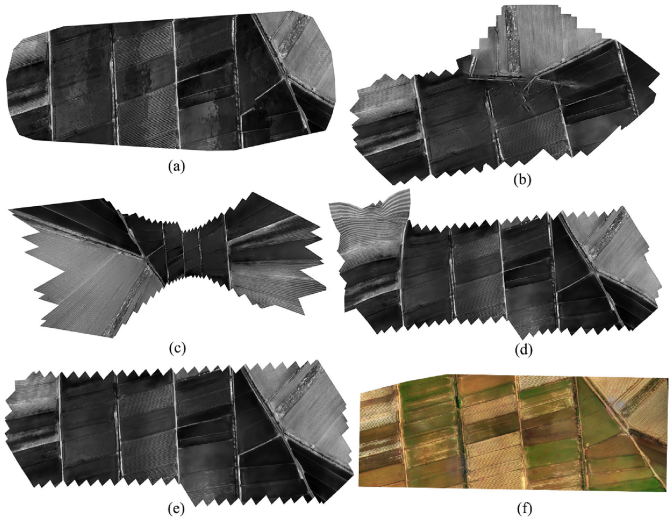

Fig. 1. Image stitching illustration of 100 UAV TIRS images. (a) Pix4Dmapper. (b) PTGui. (c) AutoStitch. (d) Original GSP. (e) Ours. (f) Visible image of study area.

TABLE I
ACRONYMS OF ARTICLES

Full name of noun	Acronyms
unmanned aerial vehicle	UAV
thermal infrared remote sensing	TIRS
position and orientation system	POS
global similarity prior	GSP
As-Projective-As-Possible	APAP
field of view	FOV
ground sampling distance	GSD
overlap prior based GSP model	OP-GSP
root mean squared error	RMSE

methods mainly focus on stitching visible images. The classic image stitching methods such as AutoStitch [20] use a global homography transformation matrix mapping images to the same reference plane, given that the scene has limited depth changes and the camera has a fixed projection center [21]. However, in the actual data acquisition process, these requirements are difficult to satisfy, which usually cause image stitching dislocation, distortion, and other problems. In recent years, stitching methods based on local affine transformation [21]–[24] have attracted more and more attention. As-projective-as-possible (APAP) [22] estimates a set of smooth transformations by moving direct linear transformation, which improves the ability of local alignment, but it is easy to cause distortion when the amount of image dataset is large. The shape-preserving half-projective stitching algorithm [23] combines projective transformation and similarity transformation and smoothly extrapolates the projective transformation of the overlapping region into the nonoverlapping region to reduce the image distortion problem to a certain extent; adaptive as-natural-as-possible [24] starts from shape correction, adaptively determines the image rotation angle, and uses global similarity transformation to correct the image. According to the characteristics of UAV remote sensing images, Li *et al.* [25] proposed an algorithm to efficiently detect optimal seamlines for mosaicking aerial images captured from different viewpoints and for mosaicking street-view panoramic images without a precisely common center in a graph cut energy minimization framework. The multiple-image mosaic of UAV visible remote sensing images is reported, which is not verified on the stitching of UAV TIRS images. In [26], the parallax tolerant image mosaic method based on robust elastic warping [27] is applied to the UAV image mosaic, and the local preserved feature matching [28] is used to effectively remove the outliers in the UAV image. The recent global similarity prior (GSP) model proposed by Chen and Chuang [29] considers three constraints of image alignment, local similarity, and global similarity simultaneously and significantly improves the quality of multiple image stitching.

The existing stitching methods can achieve good results when stitching small-scale TIRS images. However, for large-scale ones, the quality of stitching is significantly reduced. Fig. 1(c) shows that the stitched result of AutoStitch is seriously distorted, and the top left corner in Fig. 1(d) shows that the stitched result of the GSP method has obvious distortion although its overall result is relatively better than the above three methods. According to the observation, the poor stitching quality of the thermal infrared images is mainly due to the accumulation of local alignment errors during the matching of adjacent images, which eventually leads to global deformation or even failure. Therefore, adding more reliable matching pairs constraint on each image in the process of image stitching will help to suppress the influence of local error of a small number of unreliable matching pairs on the overall stitching quality.

In this work, to provide reliable thermal infrared data in the study area for the related application research, we make full use of the prior information during UAV flight and propose a robust large-scale TIRS image stitching method to obtain a high-quality panoramic image. First, the prior POS information during UAV flight and camera imaging parameters are used to estimate the overlap ratio of adjacent image pairs. Second, based on them, we select reliable image pairs, which provide effective prior constraint information for improving local image alignment capability. Finally, they are integrated into the alignment term of the GSP model, and then, a simple and effective stitching method for UAV TIRS images is proposed, which significantly improves the robustness and quality of image stitching. Fig. 1(e) illustrates a stitched result using the information of the overlap ratio prior. It can be seen that compared with the original GSP [see Fig. 1(d)], the stitching quality has been significantly improved. At the same time, our method consistently outperforms Pix4Dmapper, PTGui, and AutoStich.

The rest of this article is organized as follows. Section II summarizes the related work of image stitching. Section III presents the proposed method including estimation of image overlap ratio and GSP stitching method with our prior constraint. In Section IV, the stitched results of the proposed method are overall compared and analyzed. Section V concludes this article. The acronyms used in the article are shown in Table I.

II. Related Work

A. APAP Stitching Method

The APAP [25] image stitching method divides the source image into $C_1 \times C_2$ grids evenly and calculates a mapping transformation matrix for each grid. It is defined as

$$\hat{h}_* = \arg\min_h \sum\nolimits_{i=1}^{N} ||w_*^i \mathrm{a}_i h||^2 \quad \mathrm{s.t}||h|| = 1 \tag{1}$$

$$w_*^i = \max(\exp(-||x_* - x_i||^2/\sigma^2), \gamma) \tag{2}$$

where a_i is the coefficient calculated by the ith image matching point pair, h is the homography matrix of the grid projected from the source image to the reference image, and the matrix is estimated by minimizing the projection error of matched feature points. Details can be found in [25]. The weight $\{w_*^i\}_{i=1}^N \in [0, 1]$ is positively related to the geometric distance between each grid center x_* and the ith matching point x_i in the image, and σ is a scale parameter. In practice, most feature points are far away from the center of the grid, and their weights tend to 0. To avoid the loss of the contribution of these feature points, APAP offset the weight with a small value γ within 0 and 1, and it can be reexpressed as (2). In each grid, which is thought of as no parallax change, a local transformation matrix is calculated to enhance the image alignment ability. In terms of the quality of pairwise alignment, APAP has an obvious advantage.

B. GSP Stitching Method

To make the stitched result as natural as possible, the GSP [29] method takes the mesh vertex as the optimization term to construct the energy function with multiple constraints.

Let V_i and E_i denote the set of vertices and edges in the grid mesh for the image I_i, respectively. V denotes the set of all vertices in all images. The method attempts to find a set of deformed vertex positions $\tilde{\mathrm{V}}$ such that an energy function $\Psi(\mathrm{V})$ is minimized. Locally, the original perspective of each image is expected to be retained as much as possible, so that the panoramic image has better detail information. Globally, the GSP method hopes to find the appropriate scale and rotation for each image to maintain a good structure. Thus, the energy function consists of three terms: the alignment term $\Psi_a(\mathrm{V})$, the local similarity term $\Psi_l(\mathrm{V})$, and the global similarity term $\Psi_g(\mathrm{V})$. Therefore, it is defined as

$$\widetilde{\mathrm{V}} = \arg\min_{\widetilde{\mathrm{V}}} \Psi_a(\mathrm{V}) + \lambda_l \Psi_l(\mathrm{V}) + \Psi_g(\mathrm{V}). \tag{3}$$

In the following, let J denote the set of adjacent image pairs, M^{ij} is the set of matching points of image I_i and I_j, and N is the number of the image to be stitched.

Alignment term $\Psi_a(\mathrm{V})$: The distance between the target position mapped by the transformation of feature points in the source image and their correspondences is minimized to ensure the image alignment quality after deformation. It is defined as

$$\Psi_a(\mathrm{V}) = \sum_{i=1}^{N} \sum_{(i,j)\in \mathrm{J}} \sum_{p_k^{ij} \in \mathrm{M}^{ij}} ||\tilde{v}(p_k^{ij}) - \tilde{v}(\Phi(p_k^{ij}))||^2 \tag{4}$$

where $\Phi(p)$ returns the correspondence for a given matching point p. The function $\tilde{v}(p)$ expresses $p's$ position as a linear combination of four vertex positions in a mesh.

Local similarity term $\Psi_l(\mathrm{V})$: The mesh in the image is expected to undergo a similarity transformation to protect the local structure of the image

$$\Psi_l(\mathrm{V}) = \sum_{i=1}^{N} \sum_{(j,k)\in \mathrm{E}_i} ||(\tilde{v}_k^i - \tilde{v}_j^i) - \mathrm{S}_{jk}^i(\tilde{v}_k^i - \tilde{v}_j^i)||^2 \tag{5}$$

where v_j^i is the position for an original vertex and $\tilde{v}_j^i$ represents the position of the vertex after deformation. S_{jk}^i is the similarity transformation for the edge (j, k), which can be represented as

$$\mathrm{S}_{jk}^i = \begin{bmatrix} c(e_{jk}^i) & s(e_{jk}^i) \\ -s(e_{jk}^i) & c(e_{jk}^i) \end{bmatrix}. \tag{6}$$

The coefficients $c(e_{jk}^i)$ and $s(e_{jk}^i)$ can be expressed as linear combinations of vertex variables. Details can be found in [30]. This constraint can minimize the alignment error of each edge in each mesh after similarity transform.

Global similarity term $\Psi_g(\mathrm{V})$: The constraint is defined as

$$\Psi_g(\mathrm{V}) = \sum_{i=1}^{N} \sum_{e_j^i \in \mathrm{E}_i} \omega(e_j^i)^2 [(c(e_j^i) - s_i \cos\theta_i)^2 + (s(e_j^i) - s_i \sin\theta_i)^2] \tag{7}$$

where s_i is the desired scale and θ_i is the rotation angle for image I_i. Since the alignment constraint similar to the image overlapping region cannot be provided in the nonoverlapping region of the image, the global similarity plays a key role in the nonoverlapping area. Therefore, the weight $\omega(e_j^i)$ is expressed as

$$\omega(e_j^i) = \beta + \frac{\gamma}{|Q(e_j^i)|} \sum_{qk \in Q(e_j^i)} \frac{d(qk, \mathrm{M}^i)}{\sqrt{R_i^2 + C_i^2}} \tag{8}$$

where $Q(e_j^i)$ is the set of quads, which share the edge e_j^i; β and γ are constants controlling the importance of the term; M^i denotes the set of quads in the overlap region of I_i; $d(qk, \mathrm{M}^i)$ returns the distance of the quad and the overlap region of I_i; and R_i and C_i denote the numbers of rows and columns in the grid mesh for I_i. It can be found from (8) that the farther away from the image overlapping area, the greater the weight corresponding to the grid edge. Details can be found in [29].

III. Proposed Method

Generally, the GSP method provides a good framework for multiple image stitching, and local alignment parameters estimated by all image matching pairs provide the initial solution of GSP. In the case of no prior information in the image sequence, the traditional method usually makes pairwise matching between each image and all other images and selects the high-confidence matching pairs. However, due to the weak features and poor quality of TIRS images, the precision of local alignment is generally not high. If the number of image matching pairs is

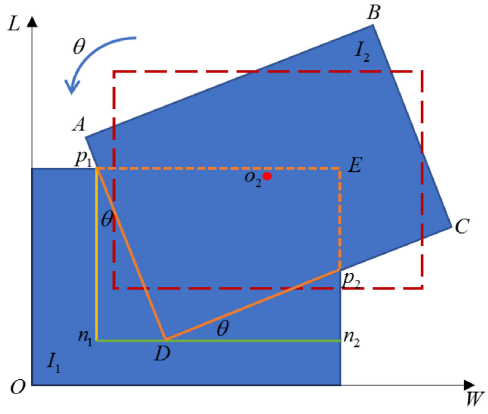

Fig. 2. Position relationship of ground FOV of two remote sensing images.

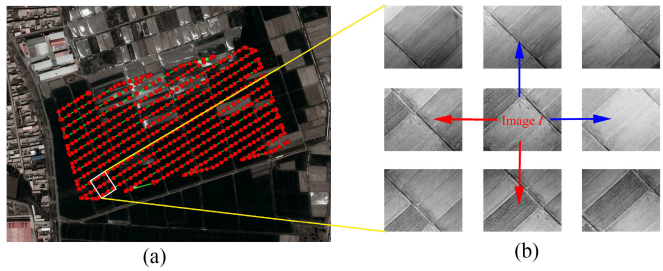

Fig. 3. Overlap ratio prior introduces more alignment constraints with different directions for each image. (a) Flight route and shooting position of UAV in the study area. (b) Examples of matching pairs for I. The red marked image pair is the best matching pair obtained by the traditional method, only using the matching relationship of two neighborhood directions. In this article, the first four adjacent image pairs with the highest overlap ratio are added to the image alignment constraint of GSP to reduce the image alignment error.

small, the stitching quality of the GSP method is difficult to guarantee.

We add more reliable image matching pair constraints to the local alignment term of the GSP model, which will help to overcome the deformation and even failure caused by the imprecise matching of a few image matching pairs.

A. Overlap Estimation of UAV Remote Sensing Images

Although the front and side overlap ratio have been planned when UAV is used to obtain TIRS images, due to the influence of UAV jitter and wind, there may be different degree error between the real overlap ratio of remote sensing image and the designed one. In this article, the overlap ratio of two remote sensing images is estimated according to the POS information carried by UAV during flight (including longitude and latitude coordinates, altitude, and heading angle) combined with the internal parameters of the thermal infrared camera. In addition, considering that the UAV's posture almost only has the rotation transformation when it flies in low wind and fixed height, the changes of the yaw angle and pitch angle during UAV flight are so small that they are practically negligible. Therefore, to reduce the computational cost, we ignore their influences on the estimation of the image overlap ratio.

Assuming that the flight altitude of UAV is h, the focal length of the thermal infrared camera is f, and the pixel size is a, the ground sampling distance (GSD) is defined as

$$\text{GSD} = h * a/f. \tag{9}$$

Let $w = \text{GSD}\times row$ and $l = \text{GSD}\times col$ be, respectively, the FOV resolution of the image on the ground, where row and col are, respectively, the height and width of a single image. If the rotation angle of the adjacent UAV image sequences is θ and the longitude and latitude coordinates of the image are, respectively, expressed as (Lat_1, Lon_1) and (Lat_2, Lon_2), then the position relationship of the two adjacent images in the ground FOV is shown in Fig. 2. The coordinate system is established with the lower-left corner of the image as the origin. The red box is the FOV before UAV rotation. By using simple geometric transformation theory, its center coordinate $o_2(x_0, y_0)$ can be defined as

$$\begin{aligned} x_0 &= \pi\left(R\cos Lat_1\right)\left(Lon_2 - Lon_1\right)/180 + w/2 \\ y_0 &= \pi R\left(Lat_2 - Lat_1\right)/180 + l/2 \end{aligned} \tag{10}$$

$$\begin{bmatrix} x \\ y \\ 1 \end{bmatrix} = \begin{bmatrix} \cos\theta & -\sin\theta & -x_0\cos\theta + y_0\sin\theta + x_0 \\ \sin\theta & \cos\theta & -x_0\sin\theta - y_0\cos\theta + y_0 \\ 0 & 0 & 1 \end{bmatrix} \begin{bmatrix} x' \\ y' \\ 1 \end{bmatrix}. \tag{11}$$

Therefore, according to the principle of image affine transformation, the coordinate $(x,' y')$ after rotation of any point (x, y) in the original position is expressed as (11); thus, the coordinates of four vertices A, B, C, and D of the rotated image I_2 can be calculated, expressed as $\mathrm{A}(x_A,y_A)$, $\mathrm{B}(x_B,y_B)$, $\mathrm{C}(x_C,y_C)$, $\mathrm{D}(x_D,y_D)$. Therefore, let p_1 and p_2 be the intersections of FOVs corresponding to two adjacent images; it can be expressed as

$$\begin{aligned} &p_1\left((l - y_D)\cdot(x_A - x_D)/(y_A - y_D) + x_D, l\right) \\ &p_2\left(w,\ (w - x_D)/(x_C - x_D)\cdot(y_C - y_D) + y_D\right). \end{aligned} \tag{12}$$

Then, the overlap ratio between two adjacent images η can be defined as

$$\begin{aligned} \eta = &\frac{|p_1 - E| * |p_1 - n_1| - 1/2|p_1 - n_1| * |p_1 - D|\sin\theta}{w * l} \\ &- \frac{1/2|D - n_2| * |p_2 - D|\sin\theta}{w * l}. \end{aligned} \tag{13}$$

As shown in Fig. 3(a), each image of UAV TIRS images contains the spatial position relationship of front and side direction. The overlap ratio between any two images can be calculated by (13), and the image matching pair is added to the alignment constraint of the GSP model so that the image alignment constraint of each image is increased from two directions to four directions. The red marked image matching in Fig. 3(b) is the best matching pair in two directions estimated by traditional methods (each image in the data set is matched with other images, and the confidence level of image matching is recorded, and the image matching pair to be retained is selected according to the reliability of matching configuration). Obviously, fewer orientation constraints may easily lead to stitching dislocation or even distortion. According to the overlap ratio prior information,

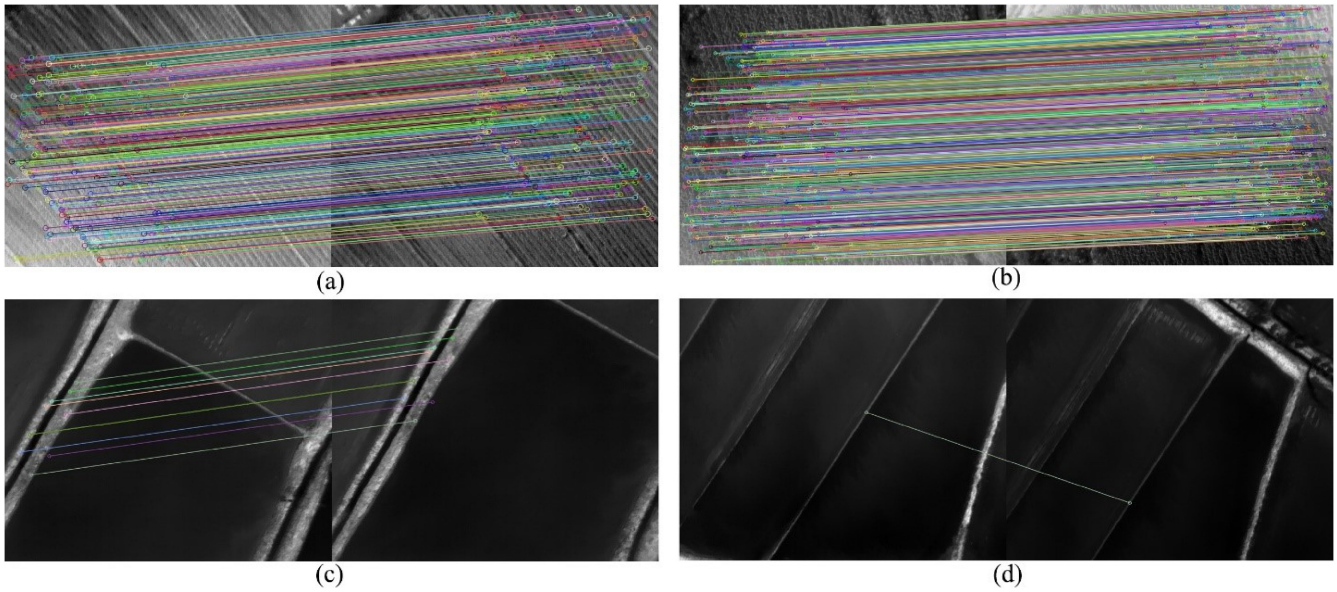

Fig. 4. Examples of matching mapping of feature points between four images pairs with a high overlap ratio. In (a) and (b), there are a large number of matching point pairs and its reliability is high. In (c) and (d), the number of feature point matching pairs is less, so its reliability becomes low.

two additional image matching pairs [as shown in the blue line in Fig. 3(b)] can be obtained, so as to construct four image matching pair constraints in different directions for the image. More diverse constraints can suppress the distortion caused by inaccurate matching pair and then avoid the stitching falling into the local optimal solution.

B. Overlap-Prior-Based GSP Stitching Method

Many image matching pairs with different directions are constructed for each image according to the overlap between it and adjacent ones. However, not all image pairs with a high overlap ratio can improve the stitching effect. For example, Fig. 4 shows four examples of feature point mapping between adjacent image pairs with a high overlap ratio. The first two groups [see Fig. 4(a) and (b)] have a large number of matching point pairs, and their distribution is relatively uniform, so they have high confidence. On the contrary, in the latter two groups, the number of matching points is small and the distribution is concentrated, and their matching is obviously unreliable. Then, if they are used to stitching, the corresponding result is made worse. Therefore, we only add those image pairs, whose number of feature point matching pairs (using the RANSAC [31] method to eliminate mismatched feature points) is greater than a certain threshold, to the local alignment term of the GSP model.

After selecting appropriate image pairs, we consider that the higher the overlap ratio between images, the greater the influence of image matching pair on the weight of alignment constraint. Therefore, the overlap ratio is used as the weight of image matching pairs in alignment term; the alignment term after increasing the overlap ratio constraint can be defined as

$$\Psi_a^{\mathrm{op}}(\mathrm{V}) = \sum_{i=1}^{N} \sum_{(i,j)\in \mathrm{J}} \sum_{p_k^{ij}\in \mathrm{M}^{ij}} \eta_{ij} ||\tilde{v}(p_k^{ij}) - \tilde{v}(\Phi(p_k^{ij}))||^2. \quad (14)$$

Therefore, the objective function of the overlap-ratio-prior-based GSP model (OP-GSP) can be expressed as

$$\tilde{\mathrm{V}}' = \arg\min_{\tilde{\mathrm{V}}} \Psi_a^{\mathrm{op}}(\mathrm{V}) + \lambda_l \Psi_l(\mathrm{V}) + \Psi_g(\mathrm{V}). \quad (15)$$

Similar to the original GSP, our method can also be solved by using a standard least squares optimization method such as conjugate gradient, and the positions of all mesh vertexes of each image in the reference plane can be obtained.

IV. Results and Discussions

A. Dataset and Evaluation Index

1) Dataset: The study was carried out in the Shahaoqu subdistrict of Hetao irrigation district, Inner Mongolia, China. This area is located at $40°52'\sim 41°00'$ N and $107°05'\sim 107°10'$ E, with a total area of 52.4 km^2. It is located in the transition zone between arid and semiarid, desert and grassland. It has the characteristics of mid temperate plateau and continental climate. It has dry climate and large evaporation. The study area consists of four fields, namely, Field 1, Field 2, Field 3, and Field 4, which range from 150 000 to 250 000 m^2. The soil salinity in the study area is higher, and the soil salinization is more serious. The salt content of the four study areas is gradually increasing, among which the salt content of Field 1 is the lowest and that of Field 4 is the highest. The land feature information of the study area mainly includes crops (sunflower, corn, and wheat), plastic mulched farmland, and uncultivated land, among which sunflower has the largest planting area. The location map of the study area is shown in Fig. 5.

The acquisition devices were Jingwei M600 UAV and the Zenmuse XT thermal infrared camera system [the resolution of each image is 640 × 512 and the GSD is 129.52 mm (at 100 m altitude)] produced by SZ DJI, China. The TIRS images

TABLE II
ACQUISITION PARAMETERS OF UAV TIRS IMAGES FROM FOUR FIELDS

	Study area	Time	Weather	Number	Front Overlap	Period of duration	Height (m)
2018	Field 1	May 1 19:00	cloudy	284	70%	Seedling stage	0.45
		July 12 17:00	cloudy	368	80%	Squaring stage	1.34
		Sep 17 9:30	light rain	524	85%	Mature stage	1.64
	Field 2	May 1 18:00	cloudy	284	70%	Seedling stage	0.52
		July 16 10:15	cloudy	413	85%	Squaring stage	0.96
		Sep 17 16:37	light rain	551	85%	Mature stage	1.28
	Field 3	May 2 12:20	fine	336	70%	Seedling stage	0.3
		July 16 11:00	cloudy	558	85%	Squaring stage	1.21
		Sep 18 9:30	light rain	513	85%	Mature stage	1.81
	Field 4	May 2 10:00	fine	263	70%	Seedling stage	0.1
		July 14 11:30	fine	468	85%	Squaring stage	0.5
		Sep 18 16:40	light rain	528	85%	Mature stage	1.44
2019	Field 1	May 14 10:10	cloudy	478		Seedling stage	0.32
		July 19 10:10	cloudy	452	85%	Squaring stage	1.2
		Sep 16 9:50	cloudy	563		Mature stage	1.71
	Field 2	May 14 12:05	cloudy	479		Seedling stage	0.46
		July 22 10:45	cloudy	420	85%	Squaring stage	1.0
		Sep 17 9:45	cloudy	445		Mature stage	1.3
	Field 3	May 16 10:30	cloudy	459		Seedling stage	0.26
		July 20 10:50	cloudy	414	85%	Squaring stage	1.2
		Sep 18 10:18	light rain	470		Mature stage	1.75
	Field 4	May 16 11:30	cloudy	519		Seedling stage	0.1
		July 21 10:40	cloudy	428	85%	Squaring stage	0.62
		Sep 20 12:10	cloudy	535		Mature stage	1.33

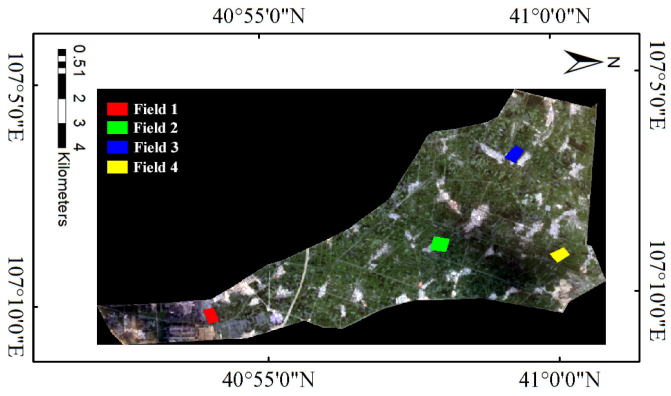

Fig. 5. Location map of the study area.

of farmland were obtained according to the planned flight route in each study area. Fig. 3(a) shows a flight route and shooting position of UAV of Field 1. The main flight parameters of UAV including altitude and speed were set as 120 m and 7 m/s, respectively.

The UAV TIRS images were taken in 2018 and 2019. Taking the growth period of sunflower as a reference, remote sensing images were obtained at different growth stages (seedling stage, squaring stage, and mature stage). In order to analyze the sensitivity of our method to different terrain height, different time, and different illumination, the TIRS images were obtained in different times of a day (including morning, noon, and afternoon) and three weather environments (sunny day, cloudy, and light rain). The specific time, quantity, and meteorological environment of TIRS images obtained in each study area are shown in Table II, and the spatial resolution at 120 m is 155.42 mm.

2) Evaluation Index of Image Stitching Quality: The evaluation of stitched results mainly includes two methods: subjective experience evaluation and objective evaluation. Subjective evaluation is based on human visual subjective evaluation, mainly including stitched results whether there is dislocation, the boundary transition is smooth, there is obvious distortion in the image, and the image details are fuzzy.

At present, the root mean squared error (RMSE) is widely used for quantitative analysis of stitched results [22]. Let G be the set of image matching pairs. For an image matching pair (I_i, I_j) in G, the position of all image matching point pairs in the reference plane is defined as $\{\tilde{p}_m^{I_i}, \tilde{p}_m^{I_j}\}_{m=0}^{N_{I_iI_j}}$, and $N_{I_iI_j}$ is the number of image matching point pairs. The RMSE calculates the average error of matching point pairs after the image pair is optimized and mapped by the method. It is defined as

$$\mathrm{RMSE} = \sqrt{\frac{\sum_{(I_i,I_j)\in G}\sum_{m=0}^{N_{I_iI_j}} ||\tilde{p}_m^{I_i} - \tilde{p}_m^{I_j}||}{\sum_{(I_i,I_j)\in G} N_{I_iI_j}}}. \quad (16)$$

This index can well evaluate the quality of the overall image alignment.

B. Experimental Results

On 24 groups of TIRS images to stitch from four study areas, we compare our method with two representative image stitching

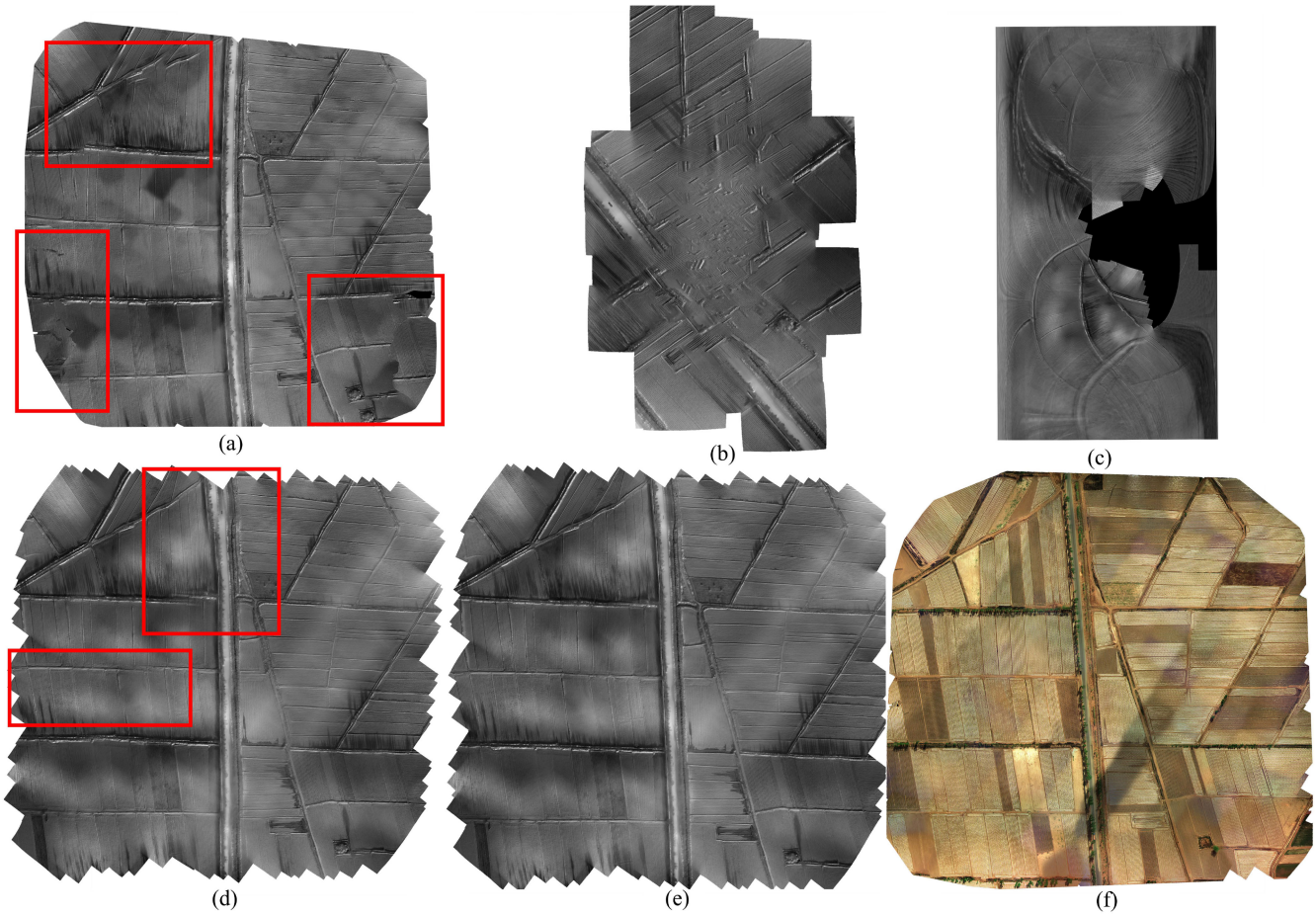

Fig. 6. Stitched result of Field 2 on the afternoon of May 1, 2018 in cloudy weather (284 images with 70% front image overlap). The red boxes indicate the mosaic dislocation and distortion. (a) Pix4Dmapper. (b) PTGui. (c) AutoStitch. (d) Original GSP. (e) OP-GSP. (f) Visible image of study area.

methods (AutoStitch [20] and GSP [29]) and two commercial stitching tools (Pix4Dmapper [13] and PTGui [14]). The experiments were performed on a computer with 3.4-GHz CPU and 8-GB RAM. SIFT features were extracted using VLFeat library [32]. According to a lot of experimental analysis, the threshold for deleting unreliable image matching pairs with high overlap ratio but low matching confidence is set to 60 (see Section III-B). All comparisons can be found in supplementary material, and the image stitching tool we developed will also be available. Refer to the first part of supplementary material for parameter setting of two commercial tools. Figs. 6 and 7 show two examples of stitched results and the comparison of local details.

1) Comparisons With the Commercial Stitching Tools: We compare our methods with two commercial tools: Pix4Dmapper and PTGui. In all experiments, we adjust different parameter settings for Pix4Dmapper and PTGui in order to get their best stitched results. In many experiments, it is found that when Pix4Dmapper and PTGui are used for TIRS image stitching, the front overlap ratio is about 85% to give a relatively good stitched result. However, because the images are not completely aligned, a high overlap ratio easily leads to image distortion. Moreover, PTGui has poor image registration ability, which easily leads to intolerable shape distortion and hole in stitched results. It is often necessary to manually select image matching pairs and select enough matching feature points between image matching pairs.

Figs. 6(a) and (b) and 7(a) and (b), respectively, show the stitched results of Field 3 and Field 2 using Pix4Dmapper and PTGui. It can be seen that although Pix4Dmapper has less distortion, the color distortion of the panoramic image is serious, and there are more local dislocation phenomena [see Fig. 6(a)]. At the same time, the edge of the image is lost seriously, and more image details cannot be retained [see Fig. 7(a)]. The results of PTGui easily lead to serious distortion and hole [see Figs. 6(b) and 7(b)]. Observing the stitched results, it can be found that our method is superior to the Pix4Dmapper and PTGui in the preservation of image detail information.

2) Comparisons With the Stitching Methods: For AutoStitch, each image adopts a global homography matrix and maps it to the reference plane by spherical projection. It is easy to cause serious distortion in nonoverlapping region of image matching pair. Because the original GSP model adopts the conventional method of constructing image matching pairs, the number of image matching pairs is less, which is easy to cause the problem of local dislocation of stitched results.

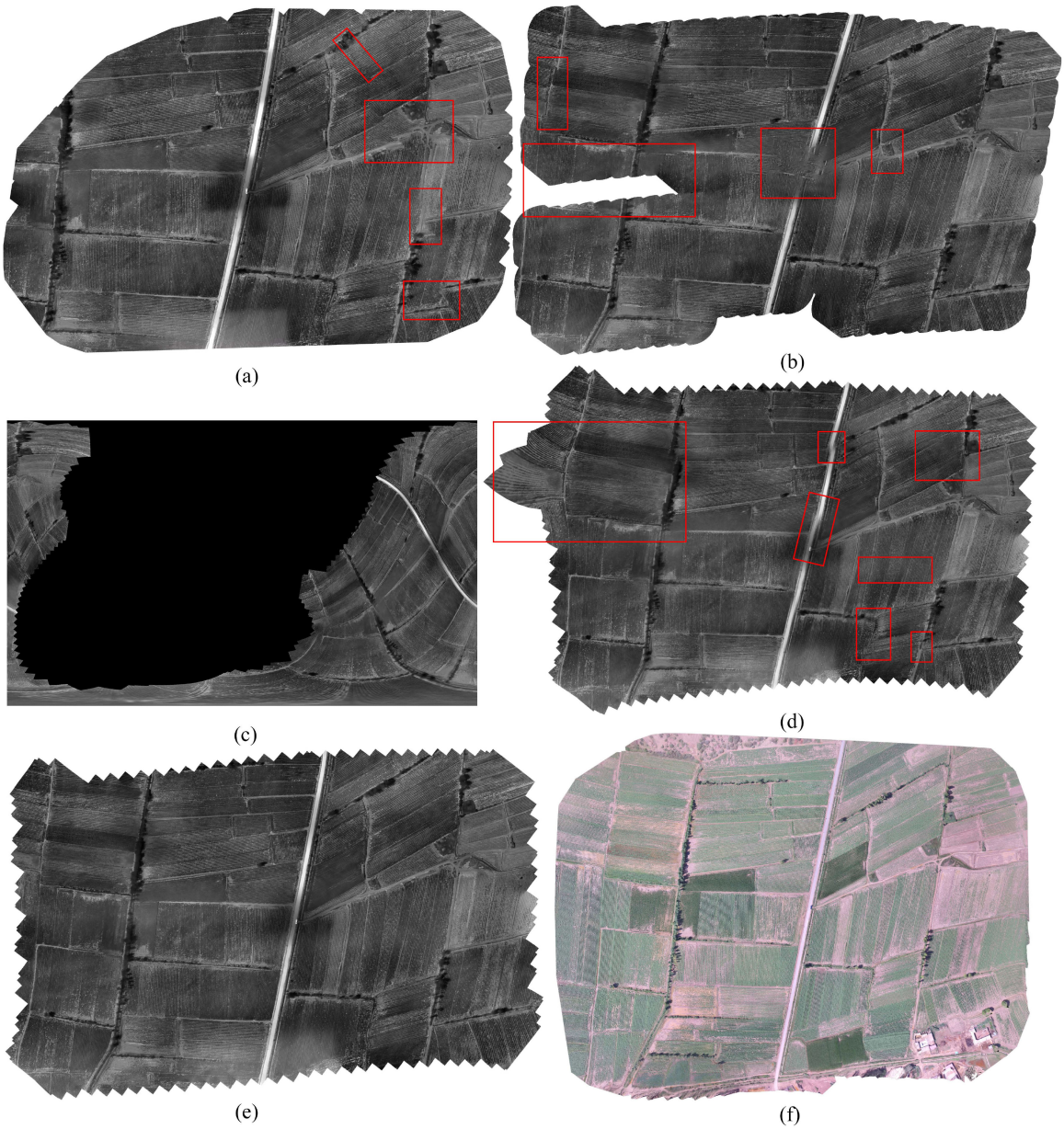

Fig. 7. Stitched result of Field 3 on the morning of July 20, 2019 in cloudy weather (414 images with 85% front image overlap). The red boxes indicate the mosaic dislocation and distortion. (a) Pix4Dmapper. (b) PTGui. (c) AutoStitch. (d) Original GSP. (e) OP-GSP. (f) Visible image of study area.

Comparison with the visible panoramic images of the study area (result from Pix4Dmapper) in the same period [see Figs. 6(f) and 7(f)], it can be found that AutoStitch's results exhibit heavy image shape distortions [see Figs. 6(c) and 7(c)]. The original GSP method is superior to AutoStitch in image distortion, but due to poor quality of image alignment and lack of overlap ratio prior information, dislocations occur to varying degrees in stitched results [see Figs. 6(d) and 7(d)]. Our method is superior to AutoStitch in image shape distortion and misalignment and is more robust than original GSP in the ability of image alignment [see Figs. 6(e) and 7(e)].

3) Comprehensive Evaluation: Tables III and IV show the stitched results of 24 groups of UAV TIRS data in 2018 and 2019. It is found that commercial tools Pix4Dmapper and PTGui cannot guarantee high-quality stitched results whether in the morning or the afternoon, or on sunny days or cloudy days, and there are several groups of data whose stitching results are serious distorted or even unsuccessful. Our method only fails to stitch the data of Field 1 in July 2019. The reason is that the TIRS images were severely exposed, resulting in the inability to extract enough feature points for matching. Compared with GSP, the proposed method achieves better stitched results on the other 23 groups of TIRS images data under different meteorological conditions and crop growth periods, which verifies the robustness of our method.

Furthermore, we compute the RMSE to quantify the alignment accuracy of the image stitching result. Because the commercial tools cannot add a module to calculate RMSE, we only

TABLE III
EVALUATION AND COMPARISONS OF STITCHING RESULTS ON 12 GROUPS OF UAV TIRS IMAGES IN 2018

Experimental Environment				Pix4Dmapper	PTGui	AutoStitch	GSP	OP-GSP (Ours)
fine	morning May	*Field 4*	**-Result**	Holes	Dislocation	Distortion	Dislocation	Success
			-RMSE	—	—	—	1.90883	**0.866687**
	morning July	*Field 4*	**-Result**	Success	Success	Distortion	Dislocation	Success
			-RMSE	—	—	—	1.32339	**0.677089**
	noon May	*Field 3*	**-Result**	Success	Dislocation	Distortion	Dislocation	Success
			-RMSE	—	—	—	1.44841	**0.767659**
cloudy	morning July	*Field 2*	**-Result**	Dislocation	Dislocation	Distortion	Dislocation	Success
			-RMSE	—	—	—	1.53082	**0.72491**
	morning July	*Field 3*	**-Result**	Failed	Dislocation	Distortion	Dislocation	Success
			-RMSE		—	—	2.1054	**0.752048**
	afternoon May	*Field 1*	**-Result**	Dislocation	Distortion	Distortion	Dislocation	Success
			-RMSE	—	—	—	1.55952	**0.954643**
	afternoon July	*Field 1*	**-Result**	Failed	Dislocation	Distortion	Dislocation	Success
			-RMSE		—	—	1.74037	**0.918486**
	afternoon May	*Field 2*	**-Result**	Dislocation	Distortion	Distortion	Dislocation	Success
			-RMSE	—	—	—	1.77413	**0.814871**
light rain	morning Sep	*Field 1*	**-Result**	Dislocation	Dislocation	Distortion	Dislocation	Success
			-RMSE	—	—	—	1.45784	**0.869685**
	morning Sep	*Field 3*	**-Result**	Dislocation	Dislocation	Distortion	Dislocation	Success
			-RMSE	—	—	—	2.17742	**0.86588**
	afternoon Sep	*Field 2*	**-Result**	Dislocation	Dislocation	Distortion	Success	Success
			-RMSE	—	—	—	1.12346	**0.916767**
	afternoon Sep	*Field 4*	**-Result**	Failed	Success	Distortion	Dislocation	Success
			-RMSE		—	—	1.3577	**0.771898**

Note: Dislocation indicates that there are only a few minor stitching misalignments in the result and can keep the basic structure of the image [such as Fig. 6(a)]. Distortion indicates that the image stitching result has serious deformation and cannot maintain the original structure [such as Fig. 6(c)]. Holes means some information is lost inside the image, but no dislocation and distortion occurred. Success indicates good stitching result [such as Fig. 6(e)]. In addition, the vegetation coverage was low in May and high in September.

TABLE IV
EVALUATION AND COMPARISONS OF STITCHING RESULTS ON 12 GROUPS OF UAV TIRS IMAGES IN 2019

Experimental Environment				Pix4Dmapper	PTGui	AutoStitch	GSP	OP-GSP (Ours)
cloudy	morning May	*Field 1*	**-Result**	Dislocation	Dislocation	Distortion	Dislocation	Success
			-RMSE	—	—	—	0.979356	**0.688355**
	morning May	*Field 3*	**-Result**	Failed	Dislocation	Distortion	Dislocation	Success
			-RMSE		—	—	3.08034	**0.786374**
	noon May	*Field 4*	**-Result**	Dislocation	Success	Distortion	Dislocation	Success
			-RMSE	—	—	—	1.15773	**0.59877**
	morning July	*Field 1*	**-Result**	Failed	Distortion	Failed	Failed	Failed
			-RMSE		—			
	morning July	*Field 2*	**-Result**	Failed	Dislocation	Distortion	Dislocation	Success
			-RMSE		—	—	1.9956	**0.778639**
	morning July	*Field 3*	**-Result**	Dislocation	Dislocation	Distortion	Dislocation	Success
			-RMSE	—	—	—	2.38161	**0.799122**
	morning July	*Field 4*	**-Result**	Success	Success	Distortion	Dislocation	Success
			-RMSE	—	—	—	2.03941	**0.841251**
	morning Sep	*Field 1*	**-Result**	Dislocation	Dislocation	Distortion	Dislocation	Success
			-RMSE	—	—	—	1.47778	**0.855281**
	morning Sep	*Field 2*	**-Result**	Failed	Dislocation	Distortion	Dislocation	Success
			-RMSE		—	—	1.79748	**0.779618**
	noon May	*Field 2*	**-Result**	Failed	Dislocation	Distortion	Dislocation	Success
			-RMSE		—	—	2.12599	**0.804055**
	noon Sep	*Field 4*	**-Result**	Dislocation	Dislocation	Distortion	Dislocation	Success
			-RMSE	—	—	—	2.08635	**0.76264**
light rain	morning Sep	*Field 3*	**-Result**	Failed	Distortion	Distortion	Dislocation	Success
			-RMSE		—	—	1.89367	**0.845696**

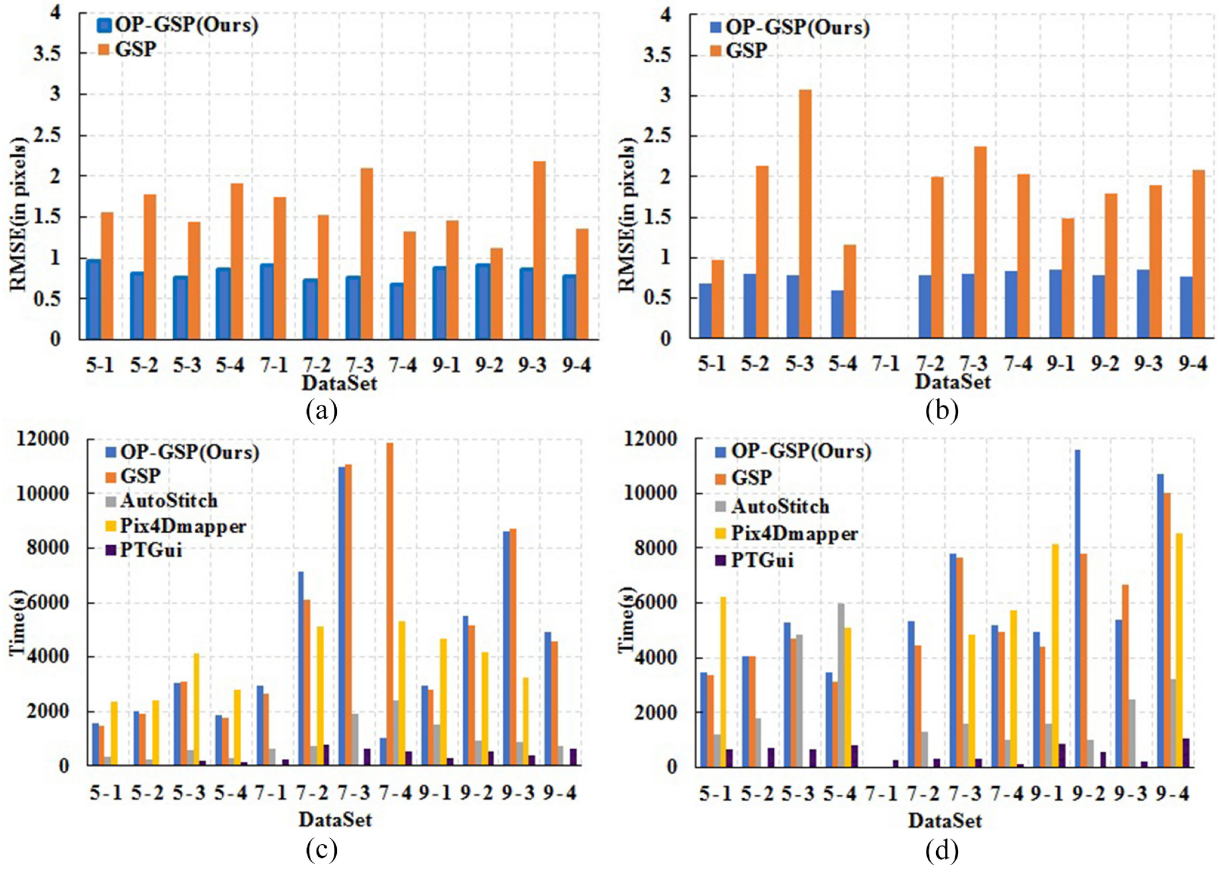

Fig. 8. RMSE and running time on the Dataset 2018 and Dataset 2019. (a) RMSE comparisons in data of 2018. (b) RMSE comparisons in data of 2019. (c) Running time comparisons in data of 2018. (d) Running time comparisons in data of 2019.

calculate the RMSE of original GSP and OP-GSP. From Fig. 8(a) and (b), it can be found that the proposed method has lower RMSE than original GSP, and the RMSE can be kept within one pixel in different meteorological conditions and crop growth periods with height of change. It can reduce image blur and make the pixel value of panoramic image closer to the real value, which is useful to carry out the follow-up research work based on the thermal infrared panoramic image.

In sum, commercial tools for image stitching have the potential to achieve better stitched results when the front overlap ratio of TIRS images is about 85%. AutoStitch uses global homography and spherical projection and may cause severe image distortion. Most panoramic images stitched by original GSP suffer from local misalignment and edge distortion. Owing to the loss of prior information of spatial location and overlap ratio of UAV remote sensing images in the optimization process, the algorithm is easy to fall into the local optimal solution. Our method incorporates overlap ratio prior information into the optimization process, obtains panoramic images that are superior to popular commercial tools and classical stitching methods, especially in protecting image details and suppressing image distortion, and is robust to ground depth, shooting time, and weather conditions. Fig. 8(c) and (d) shows the running time comparison of 24 groups of experimental data by five image stitching methods. Generally, compared to other stitching methods and commercial tools, our approach with more local alignment constraints increases the time consumption of the stitching process. In addition, when the number of remote sensing images to be stitched is small, our algorithm is faster than Pix4Dmapper, but when the number of remote sensing images to be stitched is large, the opposite is true.

C. Discussions

1) Comparison With and Without Overlap Prior Information: Fig. 9 shows an example of the GSP's stitched result without overlap ratio prior constraint, with all high-overlap ratio image pairs as constraint and with the proposed method. It can be found that there are few side constraints in the image stitching path calculated by the traditional method [see Fig. 9(a)], and the original spatial position constraint of the image is lost. The stitched result of GSP has different degrees of distortion and dislocation [see Fig. 9(d)]. The poor image quality of UAV TIRS images makes the feature point positioning not accurate. Then, fewer and inaccurate image alignment terms lead that the GSP optimization algorithm obtains the local optimal solution. However, Fig. 9(b) and (e) indicates that GSP only with high overlap ratio information cannot improve stitching quality, and it has no advantages over the original GSP without overlap prior. Finally, our method by selecting reliable image pairs [see Fig.

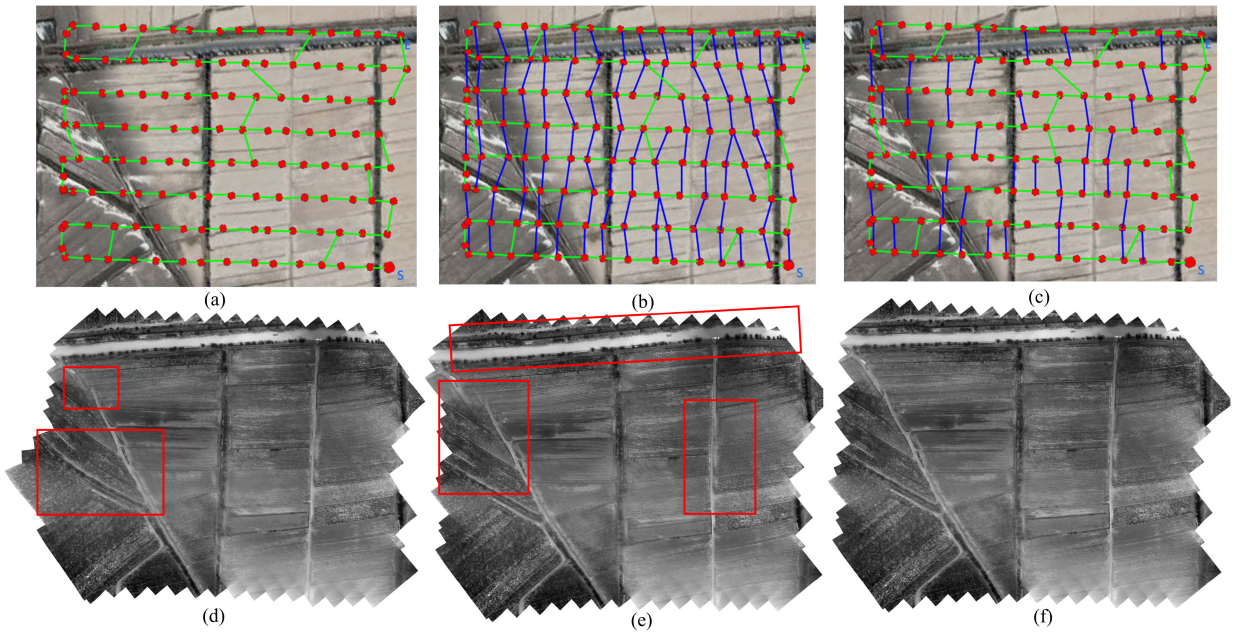

Fig. 9. Examples of image stitched results with or without overlap ratio prior information. (a) Path of image stitching calculated by the traditional method (marked by green lines). (b) Path of image stitching with all high overlap ratio image matching pairs (marked by blue lines). (c) Path of image stitching with selected reliable image matching pairs with high overlap ratio and high matching confidence (our method). (d) Stitched result of GSP according to (a). (e) Stitched result of GSP according to (b). (f) Stitched result of our OP-GSP according to (c).

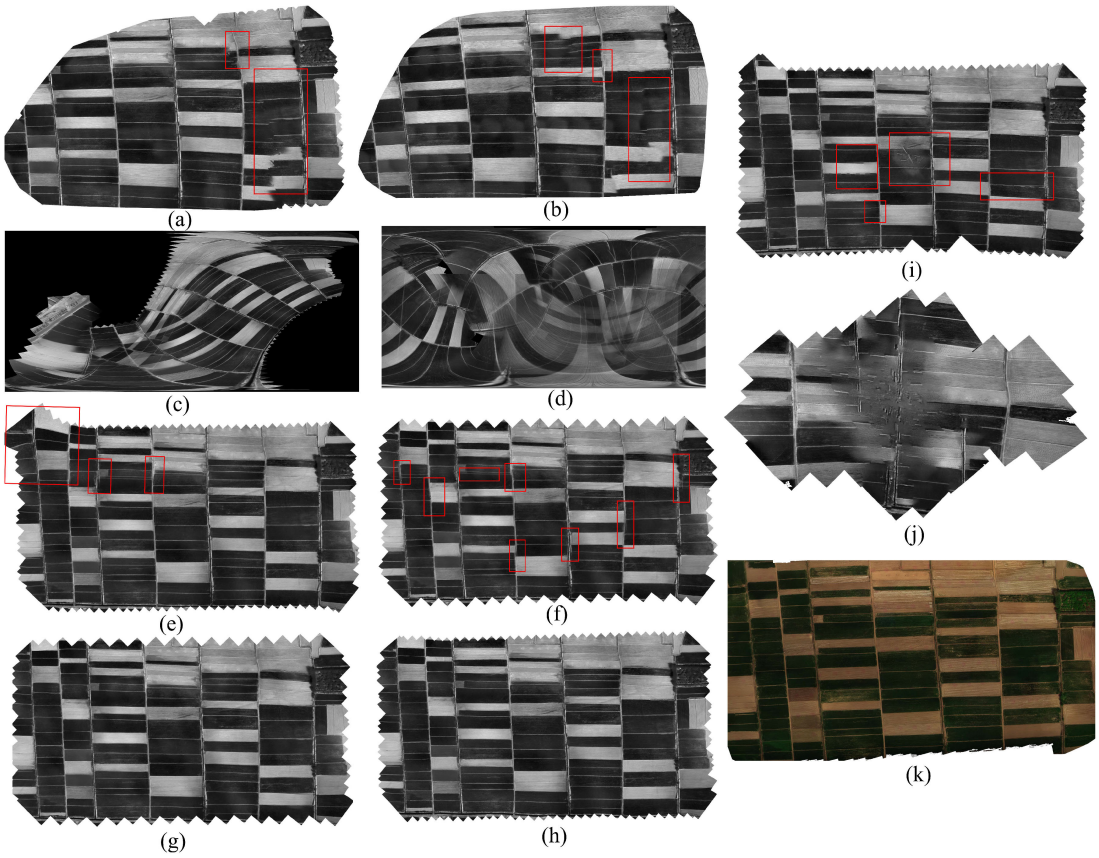

Fig. 10. Stitched results of the original front overlap ratio (85%) and the reduced overlap ratio (70%) of Field 1 in May 2019. The image stitching misalignment and distortion are marked with a red box. (a) Pix4Dmapper (85%). (b) Pix4Dmapper (70%). (c) AutoStitch (85%). (d) AutoStitch (70%). (e) Original GSP (85%). (f) Original GSP (70%). (g) OP-GSP (85%). (h) OP-GSP (70%). (i) PTGui (85%). (j) PTGui (70%). (k) Visible image of study area.

9(c)] enhances the local alignment capability of GSP and obtains better stitched result [see Fig. 9(f)] than Fig. 9(d) and (e).

2) Discussion on Reducing Front Overlap: The high overlap ratio can increase the accuracy of image registration and reduce the distortion of the nonoverlapping area. However, it will reduce the acquisition efficiency of UAV remote sensing images, and the image details are easy to blur due to the high overlap ratio. At present, the popular stitching commercial tools such as Pix4Dmapper and PTGui require the overlap ratio of TIRS images above about 85%. As a result of the fact that the images are not fully aligned [25], the higher the overlap ratio, the more likely the details of the panoramic image are blurred. It is verified by many experiments that our method can still get better stitched results when the front overlap ratio is about 70%. Fig. 10 shows the stitched results of five methods when the front overlap ratio is 70%. Fig. 10(b) shows that the stitched result of Pix4Dmapper at 70% overlap ratio has more obvious color imbalance compared with Fig. 10(a) at 85% overlap ratio. However, both PTGui and AutoStitch cause intolerable errors [see Fig. 10(d) and (f)]. Original GSP has more dislocations after reducing the front overlap ratio. Our method achieves good stitched results on two groups of image front overlap ratios.

V. Conclusion

Aiming at the challenge of large-scale UAV TIRS images stitching, for the first time, we propose a novel stitching method to obtain high-quality panoramic images by fully exploring POS data during UAV flight and parameters of thermal infrared camera. The main contributions are as follows.

First, we estimate the overlap ratio of adjacent remote sensing images by jointly using flight parameters of UAV including to longitude and latitude coordinates, altitude, heading angle, and the internal parameters of the camera. The adjacent images in different directions with high overlap ratio and high matching confidence can be obtained and then used to construct reliable local image matching pairs to enhance the capability of local alignment. We improve the GSP model by adding them into its local alignment term to avoid a local optimal solution and then stably increase the overall stitching quality. The proposed OP-GSP consistently outperforms the original GSP method except the running time.

Second, our method is extensively verified on a dataset consisting of 24 groups of TIRS images with different crop growth periods and meteorological conditions. Compared with the representative stitching methods and two popular commercial tools, the proposed method shows a significant gain in both subjective and objective stitching quality. The panoramic image obtained by the proposed method can retain more clear details, and the image distortion problem is reduced greatly, which can better maintain the original terrain structure and geomorphic information of the study area. At the same time, when we reduce the overlap ratio of TIRS images, the proposed method still shows obvious advantages over the relevant stitching methods and commercial tools, which can improve the efficiency of UAV data acquisition.

Generally, the proposed stitching method based on the overlap ratio prior robustly obtains the panoramic image with better detail preservation and less distortion. We believe that the proposed OP-GSP provides an effective and efficient solution for large-scale UAV TIRS image stitching. In the future, the proposed method will further be verified on complex environments such as large depth changes in the scene (such as mountains), different flight heights, and complex meteorological conditions.

References

[1] R. Szeliski, "Image alignment and stitching: A tutorial," *Found. Trends Comput Graph. Vis.*, vol. 2, no. 1, pp. 1–104, 2007.

[2] M. Vasterling and U. Meyer, "Challenges and opportunities for UAV-borne thermal imaging," in *Thermal Infrared Remote Sensing: Sensors, Methods, Applications*, C. Kuenzer and S. Dech, Eds. Dordrecht, The Netherlands: Springer, 2013, pp. 69–92.

[3] M. Weiss, F. Jacob, and G. Duveiller, "Remote sensing for agricultural applications: A meta-review," *Remote Sens. Environ.*, vol. 236, Jan. 2020, Art. no. 111402.

[4] P. Zarco-Tejada, V. González-Dugo, and J. Berni, "Fluorescence, temperature and narrow-band indices acquired from a UAV platform for water stress detection using a micro-hyperspectral imager and a thermal camera," *Remote Sens. Environ.*, vol. 117, pp. 322–337, Feb. 2012.

[5] G. Messina and G. Modica, "Applications of UAV thermal imagery in precision agriculture: State-of-the-art and future research outlook," *Remote Sens.*, vol. 12, no. 9, 2020, Art. no. 1491.

[6] J. Berni, P. Zarco-Tejada, G. Sepulcre-Cantó, E. Fereres, and F. Villalobos, "Mapping canopy conductance and CWSI in olive orchards using high resolution thermal remote sensing imagery," *Remote Sens. Environ.*, vol. 113, no. 11, pp. 2380–2388, Nov. 2009.

[7] C. Brenner, C. E. Thiem, H.-D. Wizemann, M. Bernhardt, and K. Schulz, "Estimating spatially distributed turbulent heat fluxes from high-resolution thermal imagery acquired with a UAV system," *Int. J. Remote Sens.*, vol. 38, nos. 8–10, pp. 3003–3026, May 2017.

[8] H. Hoffmann, H. Nieto, R. Jensen, R. Guzinski, P. Zarco-Tejada, and T. Friborg, "Estimating evaporation with thermal UAV data and two-source energy balance models," *Hydrol. Earth Syst. Sci.*, vol. 20, no. 2, pp. 697–713, Feb. 2016.

[9] T. Liu *et al.*, "Estimates of rice lodging using indices derived from UAV visible and thermal infrared images," *Agricultural Forest Meteorol.*, vol. 252, pp. 144–154, Apr. 2018.

[10] L. Feng, H. Tian, Z. Qiao, M. Zhao, and Y. Liu, "Detailed variations in urban surface temperatures exploration based on unmanned aerial vehicle thermography," *IEEE J. Sel. Top. Appl. Earth Observ. Remote Sens.*, vol. 13, pp. 204–216, 2020.

[11] Q. Weng, "Thermal infrared remote sensing for urban climate and environmental studies: Methods, applications, and trends," *J. Photogrammetry Remote Sens.*, vol. 64, no. 4, pp. 335–344, 2009.

[12] M. Khoshboresh Masouleh and R. Shah-Hosseini, "Development and evaluation of a deep learning model for real-time ground vehicle semantic segmentation from UAV-based thermal infrared imagery," *ISPRS J. Photogrammetry Remote Sens.*, vol. 155, pp. 172–186, Jan. 2019.

[13] Pix4D, "Pix4Dmapper: Professional drone mapping and photogrammetry software—Pix4D," 2020. [Online]. Available: https://www.pix4d.com/product/pix4dmapper-photogrammetry-software

[14] New House Internet Services BV, "Photo stitching software 360 degree Panorama image software—PTGui Stitching Software," 2020. [Online]. Available: https://www.ptgui.com/

[15] J. Kelly *et al.*, "Challenges and best practices for deriving temperature data from an uncalibrated UAV thermal infrared camera," *Remote Sens.*, vol. 11, no. 5, Mar. 2019, Art. no. 567.

[16] R. Boesch, "Thermal remote sensing with UAV-based workflows," *Int. Arch. Photogrammetry, Remote Sens. Spatial Inf. Sci.*, vol. XLII-2/W6, pp. 41–46, Aug. 2017.

[17] A. Sledz, J. Unger, and C. Heipke, "Thermal IR Imaging: Image quality and orthophoto generation," *Int. Arch. Photogrammetry, Remote Sens. Spatial Inf. Sci.*, vol. XLII-1, pp. 413–420, Sep. 2018.

[18] C. Webster, M. Westoby, N. Rutter, and T. Jonas, "Three-dimensional thermal characterization of forest canopies using UAV photogrammetry," *Remote Sens. Environ.*, vol. 209, pp. 835–847, May 2018.

[19] Pix4D, "Processing thermal images," 2020. [Online]. Available: https://support.pix4d.com/hc/en-us/articles/360000173463-Processing-the rmal-images
[20] M. Brown and D. G. Lowe, "Automatic panoramic image stitching using invariant features," *Int. J. Comput. Vis.*, vol. 74, no. 1, pp. 59–73, Apr. 2007.
[21] W.-Y. Lin, S. Liu, Y. Matsushita, T.-T. Ng, and L.-F. Cheong, "Smoothly varying affine stitching," in *Proc. IEEE Conf. Comput. Vis. Pattern Recognit.*, Jun. 2011, pp. 345–352.
[22] J. Zaragoza, T. Chin, Q. Tran, M. S. Brown, and D. Suter, "As-projective-as-possible image stitching with moving DLT," *IEEE Trans. Pattern Anal. Mach. Intell.*, vol. 36, no. 7, pp. 1285–1298, Jul. 2014.
[23] C.-H. Chang, Y. Sato, and Y.-Y. Chuang, "Shape-preserving half-projective warps for image stitching," in *Proc. IEEE Conf. Comput. Vis. Pattern Recognit.*, Jun. 2014, pp. 3254–3261.
[24] C.-C. Lin, S. U. Pankanti, K. N. Ramamurthy, and A. Y. Aravkin, "Adaptive as-natural-as-possible image stitching," in *Proc. IEEE Conf. Comput. Vis. Pattern Recognit.*, Jun. 2015, pp. 1155–1163.
[25] L. Li, J. Yao, X. Lu, J. Tu, and J. Shan, "Optimal seamline detection for multiple image mosaicking via graph cuts," *ISPRS J. Photogrammetry Remote Sens.*, vol. 113, pp. 1–16, 2016.
[26] L. Luo, Q. Wan, J. Chen, Y. Wang, and X. Mei, "Drone image stitching guided by robust elastic warping and locality preserving matching," in *Proc. IEEE Int. Geosci. Remote Sens. Symp.*, Jul. 2019, pp. 9212–9215.
[27] J. Li, Z. Wang, S. Lai, Y. Zhai, and M. Zhang, "Parallax-tolerant image stitching based on robust elastic warping," *IEEE Trans. Multimedia*, vol. 20, no. 7, pp. 1672–1687, Jul. 2018.
[28] J. Ma, J. Jiang, H. Zhou, J. Zhao, and X. Guo, "Guided locality preserving feature matching for remote sensing image registration," *IEEE Trans. Geosci. Remote Sens.*, vol. 56, no. 8, pp. 4435–4447, Aug. 2018.
[29] Y.-S. Chen and Y.-Y. Chuang, "Natural image stitching with the global similarity prior," in *Proc. Eur. Conf. Comput. Vis.*, 2016, pp. 186–201.
[30] T. Igarashi and Y. Igarashi, "Implementing as-rigid-as-possible shape manipulation and surface flattening," *J. Graph., GPU, Game Tools*, vol. 14, no. 1, pp. 17–30, Jan. 2009.
[31] M. A. Fischler and R. C. Bolles, "Random sample consensus: A paradigm for model fitting with applications to image analysis and automated cartography," in *Readings in Computer Vision: Issues, Problems, Principles, and Paradigms*. San Francisco, CA, USA: Morgan Kaufmann, 1987, pp. 726–740.
[32] A. Vedaldi and B. Fulkerson, "Vlfeat," in *Proc. Int. Conf. Multimedia*, 2010, p. 1469.

Jiguang Cui is currently working toward the master's degree with the College of Information Engineering, Northwest A&F University, Yangling, China.

His current research interests include computer vision and image analysis.

Man Liu is currently working toward the master's degree with the College of Information Engineering, Northwest A&F University, Yangling, China.

Her current research interests include computer vision and image analysis.

Zhitao Zhang was born in Shaanxi, China, in 1976. He received the master's degree in engineering and the Ph.D. degree in hydrology and water resources engineering from Northwest A&F University, Yangling, China, in 2005 and 2011, respectively.

He is currently an Associate Professor with the College of Water and Construction Engineering, Northwest A&F University. His current research interests include application research of remote sensing technology in hydrology, water resources and agricultural water and soil engineering, hydrology remote sensing, and optimal allocation of irrigation water resources in irrigated areas, the new technology of water-saving irrigation.

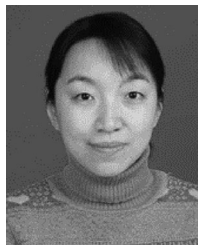

Shuqin Yang was born in Shaanxi, China, in 1978. She received the master's degree in engineering and the Ph.D. degree in agricultural electrification and automation from Northwest A&F University, Yangling, China, in 2005 and 2012, respectively.

She is currently an Associate Professor with the College of Mechanical and Electronic Engineering, Northwest A&F University. Her current research interests include image processing and analysis in agricultural information field.

Jifeng Ning was born in Shaanxi, China, in 1975. He received the master's degree in engineering from Northwest A&F University, Yangling, China, in 2002, and the Ph.D. degree in information and communication engineering from Xidian University, Xi'an, China, in 2009.

He is currently a Professor with the College of Information Engineering, Northwest A&F University. His current research interests include visual tracking and remote sensing image analysis by computer vision and machine learning.